Title
Spontaneous self-dislodging of freezing water droplets and the role of wettability.

Journal
Proceedings of the National Academy of Sciences of USA, 114(42)

Authors
Graeber, Gustav
Schutzius, Thomas
Eghlidi, Hadi
et al.

Publication Date
2017-10-17

DOI
10.1073/pnas.1705952114

Peer reviewed

Spontaneous self-dislodging of freezing water droplets and the role of wettability

Gustav Graeber[a], Thomas M. Schutzius[a,1], Hadi Eghlidi[a], and Dimos Poulikakos[a,1]

[a]Laboratory of Thermodynamics in Emerging Technologies, Department of Mechanical and Process Engineering, Eidgenössische Technische Hochschule Zürich, CH-8092 Zurich, Switzerland

Edited by Howard A. Stone, Princeton University, Princeton, NJ, and approved August 23, 2017 (received for review April 10, 2017)

Spontaneous removal of liquid, solidifying liquid and solid forms of matter from surfaces, is of significant importance in nature and technology, where it finds applications ranging from self-cleaning to icephobicity and to condensation systems. However, it is a great challenge to understand fundamentally the complex interaction of rapidly solidifying, typically supercooled, droplets with surfaces, and to harvest benefit from it for the design of intrinsically icephobic materials. Here we report and explain an ice removal mechanism that manifests itself simultaneously with freezing, driving gradual self-dislodging of droplets cooled via evaporation and sublimation (low environmental pressure) or convection (atmospheric pressure) from substrates. The key to successful self-dislodging is that the freezing at the droplet free surface and the droplet contact area with the substrate do not occur simultaneously: The frozen phase boundary moves inward from the droplet free surface toward the droplet–substrate interface, which remains liquid throughout most of the process and freezes last. We observe experimentally, and validate theoretically, that the inward motion of the phase boundary near the substrate drives a gradual reduction in droplet–substrate contact. Concurrently, the droplet lifts from the substrate due to its incompressibility, density differences, and the asymmetric freezing dynamics with inward solidification causing not fully frozen mass to be displaced toward the unsolidified droplet–substrate interface. Depending on surface topography and wetting conditions, we find that this can lead to full dislodging of the ice droplet from a variety of engineered substrates, rendering the latter ice-free.

wettability | superhydrophobicity | freezing | sublimation | icephobicity

The interaction of liquid water and ice with surfaces is fundamentally important in nature and many engineering applications (1–3). For decades researchers developed surfaces that repel water—so-called hydrophobicity—as these are promising for antifouling and self-cleaning applications (4–8). In addition, the rational design of surfaces that passively inhibit surface icing—so-called icephobicity—has gained attention in recent years, as ice affects the safety and performance of a broad palette of applications ranging from aircrafts and automobiles (transportation), to wind turbines and electrothermal energy storage (energy), and to power lines and roads (infrastructure) (9–13).

Recent investigations into the development of icephobic surfaces focused on ice nucleation delay by changing the surface topography and wettability (14, 15), ice nucleation prevention by droplet shedding due to self-propelled dropwise condensate coalescence on superhydrophobic surfaces (16), reduced contact time during droplet impact by droplet splitting (17) and pancake bouncing (18), as well as impact resistance to supercooled droplets (19). Further research studied the role of environmental conditions on the freezing process on surfaces (20, 21) and the freezing dynamics (22, 23). Despite intensive work at the complex intersection of nucleation thermodynamics, interfacial thermofluidics, and materials micro/nanoengineering, eventual freezing is often inevitable. Consequently, researchers also developed solutions to reduce ice adhesion, e.g., by liquid-infused surfaces (24). Recently, it was demonstrated that the physics of freezing dynamics at low environmental pressures can be exploited in mitigating icing by spontaneous levitation of water droplets during nonequilibrium freezing on microtextured, superhydrophobic surfaces, and guidelines for the design of surface textures conducive to this behavior were suggested (25).

Despite the progress mentioned above, in the vast majority of applications freezing water adheres and remains on surfaces, resulting in ice accretion, which is a highly undesirable event. Here we show and explain a freezing-driven ice-removal mechanism. We find that a freezing sessile water droplet, which is cooled primarily from its free surface, experiences a concentric inward growth of the phase boundary from the free surface toward the still unsolidified droplet–substrate interface. The key to successful self-dislodging is that the droplet–substrate interface remains a liquid throughout most of the process and freezes last. The volumetric expansion associated with the phase change, combined with the incompressibility of the droplet core, the flow permittivity of the still unsolidified droplet substrate interface, and the flow restriction imposed by the solid outer ice shell at the free surface, all result collaboratively in a displacement of the unsolidified core toward the substrate. Simultaneously, the inward phase-boundary motion near the substrate (ice–liquid–vapor contact line) drives a gradual reduction in droplet–substrate contact area (liquid–vapor–substrate contact line). We observe that the displaced core lifts the droplet away from the substrate, intrinsically prohibiting ice adhesion associated with freezing. Combined with further freezing and ice-shell growth, this can lead to a complete removal of the freezing droplet. We term this mechanism droplet self-dislodging, as the water droplet employs the freezing dynamics to remove itself from the substrate upon which, in the absence of this mechanism, it would be lodged. The broad range of investigated substrates and conditions is not capable of realizing the self-levitation

Significance

Freezing of water on surfaces is ubiquitous in nature and technology; however, to control ice aggregation and rationally design icephobic surfaces, which passively inhibit ice formation and accretion, a deeper fundamental understanding of the interaction of forming ice with the underlying substrate and environment is necessary. In this work, we report the phenomenon of self-dislodging freezing water droplets, explain its physics, and develop surfaces which inhibit ice aggregation through passive ice self-removal. Successful experiments on a palette of material classes underpin the general applicability and robustness of the effect to control surface icing, and can guide further research in the field of icephobicity.

Author contributions: T.M.S. and D.P. designed research; G.G. performed research; G.G., T.M.S., and H.E. contributed new analytic tools; G.G. and T.M.S. analyzed data; and G.G., T.M.S., and D.P. wrote the paper.

The authors declare no conflict of interest.

This article is a PNAS Direct Submission.

[1]To whom correspondence may be addressed. Email: dpoulikakos@ethz.ch or thomschu@ethz.ch.

This article contains supporting information online at www.pnas.org/lookup/suppl/doi:10.1073/pnas.1705952114/-/DCSupplemental.

or jumping behavior for droplets in contact with microtextured superhydrophobic surfaces discussed earlier (25). Experimentally, we study the effect of the surface–ice interaction, establish a thermofluidic model to predict the outcome of the freezing event, and deduce design rules for icephobic self-dislodging surfaces. We demonstrate the robustness and the general applicability of the self-dislodging process on a broad range of material groups, i.e., polymers, ceramics, and metals, ranging from smooth and hydrophilic, to nanotextured and superhydrophobic. This work gives insight into the fundamentals of freezing on surfaces, introduces a passive, self-cleaning mechanism, and can guide the further development of hydrophobic and icephobic materials.

Results and Discussion

We investigated freezing-driven self-dislodging of supercooled water droplets from engineered substrates; droplets were cooled via evaporation and froze from a supercooled state in a low-pressure, low-humidity environment [partial pressure of water $p_V = O(1\ \text{mbar})$, *Evaporative Cooling*]. We performed the experiments in an environmental chamber at room temperature (*Materials and Methods*). Fig. 1 shows an image sequence of a freezing water droplet, from an initially supercooled state, on a smooth [root-mean-square roughness $O(1\ \text{nm})$], hydrophobic glass substrate. Fig. 1*A* (side view) and Fig. 1*B* (bottom view) are synchronized; time zero is defined as the moment when freezing starts. The freezing of the supercooled droplet proceeds in two distinct stages (26). During the first stage (recalescence), which is relatively short [duration $O(0.01\ \text{s})$], the droplet rapidly heats up adiabatically from $T = -15 \pm 5$ °C to $T = 0$ °C (equilibrium temperature, Fig. S1), resulting in a slushy mix of solid ($\phi \approx 20$ wt. %) and liquid ($(1-\phi) \approx 80$ wt. %) water; ϕ is the solid mass divided by the total mass and depends on the degree of supercooling (14) (*Recalescence Freezing*). In the second, longer stage [classical freezing; duration $O(1\ \text{s})$], the remaining liquid water solidifies at $T = 0$ °C. Fig. 1 *A* and *B* show that further droplet freezing—that is, an increase in the thickness of the outer ice shell that proceeds radially inward from the free surface ($r_S - r_F$)—is associated with a reduction in the droplet–substrate contact radius, x_C. Here, r_S and r_F are the radial positions of the outer and inner phase boundaries, respectively. The bottom-view images reveal that the ice beyond x_C no longer contacts the substrate. The low adhesion due to the lack of contact is obvious in the end of Movie S1, where the frozen droplet slides over the substrate. Fig. 1*C* shows an example of what we identified as the ice shell (clear) and slushy core (opaque). Fig. 1*D* and Movie S1 show unequivocally that while freezing is occurring, a continuous intervening liquid layer (ILL) is maintained between freezing droplet and substrate—due to the warmer environment ($T_\infty \approx 23$ °C) and also substrate ($T_{sub} > 0$ °C)—as identified by the strong interference patterns near the contact line. We determined the thickness of this layer to be $O(10\ \mu\text{m})$ (*ILL*). The simultaneous reduction in x_C and increase in $(r_S - r_F)$ with time t is plotted in Fig. 1*E*. The total time for the droplet to self-dislodge from the substrate is defined as t_{SD}.

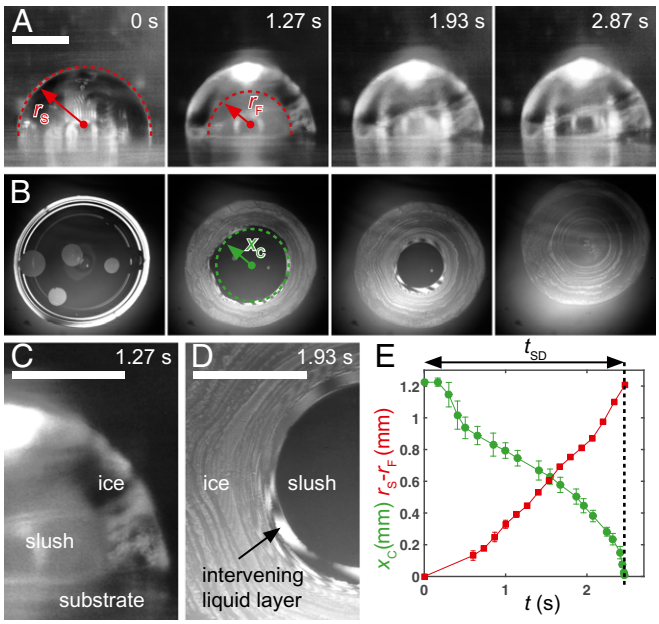

Fig. 1. Phenomenon of self-dislodging. Synchronized (*A*) side- and (*B*) bottom-view image sequences of a water droplet freezing—through evaporative cooling—on a hydrophobic glass substrate (Movie S1). (*C*) Magnified side view of a partially solidified droplet from the image sequence in *A*. Note the ice (transparent) and slush (opaque) regions. The red dashed lines in *A* indicate the outer droplet radius, r_S, and the radial position of the ice–slush phase boundary, r_F. The green dashed line in *B* indicates the droplet–substrate contact radius, x_C. (*D*) Magnified bottom view of a partially solidified droplet from the image sequence in *B*. The black arrow highlights interference patterns. (*E*) Contact radius, x_C, and ice-shell thickness, $(r_S - r_F)$, vs. time, t. The self-dislodging time, t_{SD}, is defined from the start of freezing ($t = 0$ s) until $x_C = 0$. The initial droplet volume is 5 μL. The four small circular features visible in the first image of *B* are vapor bubbles. [Scale bars: (*A*–*C*) 1.0 mm; (*D*) 0.5 mm.]

To investigate experimentally the effect of surface wettability on the dislodging behavior, we prepared three types of glass substrates with varying advancing (θ_a^*) and receding (θ_r^*) contact angles: hydrophilic ($\theta_a^* = 56 \pm 3°$, $\theta_r^* = 31 \pm 4°$), hydrophobic ($\theta_a^* = 118 \pm 3°$, $\theta_r^* = 93 \pm 3°$), and superhydrophobic ($\theta_a^* = 164 \pm 1°$, $\theta_r^* = 160 \pm 2°$) (*Materials and Methods*). As mentioned above, when supercooled droplets freeze, they undergo rapid warming, which can cause the droplet to strongly evaporate (20). On specially designed superhydrophobic microtextured surfaces, such vaporization can produce an overpressure between the droplet and substrate, which can overcome adhesion and initiate spontaneous levitation (25). In contrast, here we study droplet–surface interactions at low pressures on substrates with a wide range of wettability (from hydrophilic to superhydrophobic) and topography [from $O(1\ \text{nm})$ to $O(100\ \text{nm})$ root-mean-square roughness]. Due to their composition and structure, these substrates are unable to support high-vapor pressures and droplet self-levitation behavior, revealing dislodging as the dominant ice-shedding mechanism persisting over a broad range of wettability (*Droplet–Substrate Interactions at Low Pressure*). On the three substrates studied here, the water droplets froze repeatedly, but showed different dislodging performance. Fig. 2*A* shows an image sequence of a droplet freezing on hydrophilic glass, where we observe only partial droplet dislodging. To demonstrate this, Fig. 2*B* shows the droplet–substrate contact region (bottom view, through the transparent substrate) of a droplet on hydrophilic glass 1.5 s after freezing began. Here, we highlight two regions where the droplet and substrate make contact: the center (green dashed line) and peripheral (shaded red) areas. The peripheral region remained in contact with the substrate during the freezing event and hindered the removal of the droplet (Movie S2). Fig. 2*C* shows an image sequence of a droplet freezing and dislodging from hydrophobic glass. Fig. 2*D* shows the corresponding bottom view 1.5 s after the start of freezing. In contrast to the droplet on the hydrophilic substrate, the liquid–substrate contact area remained approximately circular and in one region (green dashed line), and kept reducing itself over the course of the freezing event, leading the droplet to self-dislodge completely from the substrate in a mean dislodging time of $t_{SD} = 2.22 \pm 0.35$ s (initial droplet volume 5 μL). The above highlights the important role that wettability plays in determining if droplet dislodging occurs or not. Fig. 2*E* shows an image sequence of a water droplet freezing on and dislodging from nanoroughened (≈30-nm root-mean-square roughness), superhydrophobic glass (Movie S3). The image sequence shows that the ice beyond the contact radius x_C clearly lifts from the substrate and

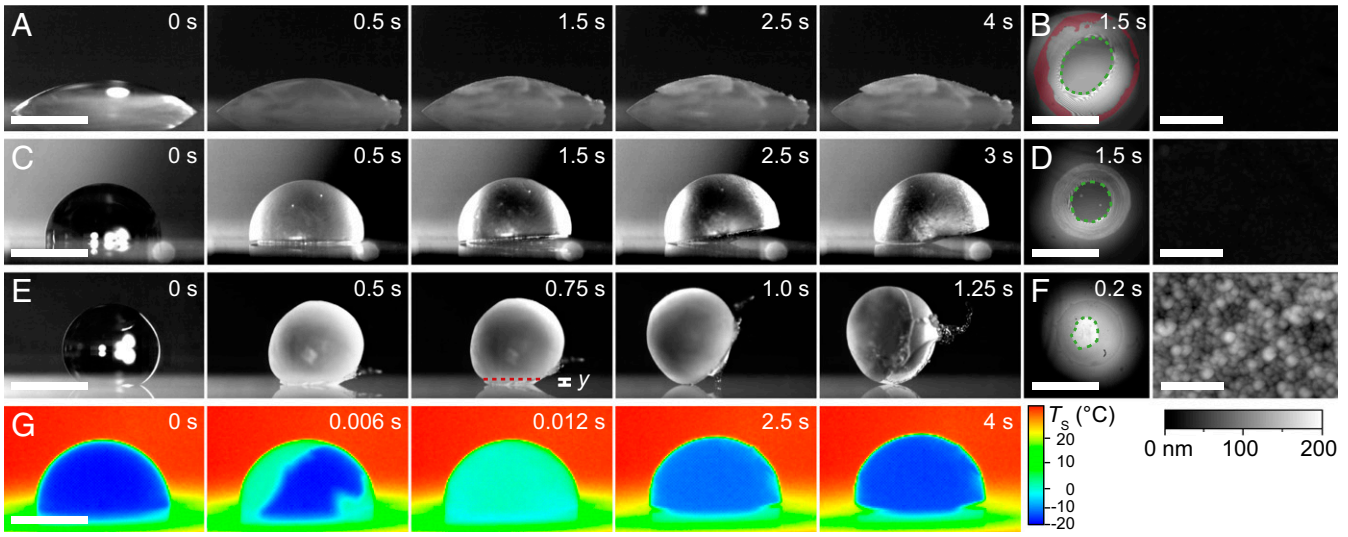

Fig. 2. Effect of substrate wettability on self-dislodging behavior. Side view of water droplets (initially 10 μL) freezing on *A*, hydrophilic (Movie S2), (*C*) hydrophobic, and (*E*) superhydrophobic glass (Movie S3), introducing the vertical lifting of the droplet *y*. Selected bottom views of droplets (initially 5 μL) freezing on (*B*) hydrophilic, (*D*) hydrophobic, and (*F*) superhydrophobic glass (Movie S4). The contact area corresponds to the region inside the green dashed line. Peripheral liquid–substrate contact area is highlighted in red. (*Insets*) Corresponding topographical scans by AFM. Gray scale bar for the height information is the same for all. (*G*) Thermographic images of a droplet self-dislodging under same conditions as *C* (Movie S5). [Scale bars: (*A*–*G*): 2 mm; *Insets*: 500 nm.]

no longer makes contact with it. Fig. 2*F* shows the bottom view of a water droplet on the superhydrophobic substrate 0.2 s after the start of freezing ($t_{SD} = 1.11 \pm 0.39$, initial droplet volume 5 μL, Movie S4). The bottom-view perspective in Movie S4 also shows how during freezing the ice beyond x_C progressively moves out of focus, indicating that it is moving away from the substrate. The droplet–substrate contact region is confined to a smaller area—relative to the hydrophilic and the hydrophobic cases—due to the increased water repellency of the substrate. Also, for a constant initial droplet volume, when supercooled droplets freeze on a substrate, t_{SD} decreases with increasing θ_a^* and θ_r^*. Fig. 2*G* presents thermographs of recalescence freezing and the self-dislodging process, allowing a noninvasive measurement of the droplet free-surface temperature, revealing its rapid increase at the moment of recalescence freezing. Of particular interest here is the subsequent surface temperature decline due to ensuing vapor sublimation (Fig. S2 and Movie S5).

To elucidate the physical mechanism responsible for the droplet self-dislodging behavior, we model the evolution of the radial position of the solid–slush phase boundary $r_F(t)$ for the case of a solidifying sphere with an initial radius, r_S. This is achieved by balancing heat removal due to sublimation from the droplet free surface, $\dot{Q}_S$, with heat generation due to phase change within the droplet, $\dot{Q}_F$ [one-phase Stefan problem (27)]. This model can be applied to any approximately spherical cap geometry in contact with a substrate, with an apparent contact angle θ_S^*—assuming that the droplet–substrate interface is adiabatic, as the associated heat rate $\dot{Q}_{sub} \ll \dot{Q}_S, \dot{Q}_F$ (Fig. S3, *Substrate Heat Transfer*, and *Spherical Cap*)—allowing us to determine the radial- $a_F(t)$, and vertical position $y(t)$, of the liquid–slush–solid–vapor quadri-junction $[s(t) = (a_F(t), y(t))]$, Fig. 3*A*. Since heat is removed from the free surface, it follows that $dr_F(t)/dt < 0$. In addition, we assumed that $y(t) \ll a_F(t)$, which holds for low values of θ_S^*, and at $\theta_S^* = 110°$, $y(t) \approx a_F(t)$, setting an upper limit for θ_S^* where the above analysis is appropriate for water (*Quadri-Junction Motion*). The assumed spherical cap geometry of the droplet and the adiabatic droplet–substrate interface justify solving the one-dimensional heat equation (spherical coordinates) for the case of a representative, inward-solidifying full sphere (r_S determined from the volume of the spherical cap and θ_S^*), and later applying the results to the investigated droplet, as

$$\frac{\partial T}{\partial t} = \alpha_{ice}\left[\frac{\partial^2 T}{\partial r^2} + \frac{2}{r}\frac{\partial T}{\partial r}\right], \qquad [1]$$

with the necessary initial $T(0, r) = T_F$ (freezing temperature of water, 0 °C), and boundary conditions,

$$T(t, r_F) = T_F,$$
$$(1-\phi)\cdot h_{F,w}\cdot \rho_{ice}\cdot \dot{r}_F = -\left[-\lambda_{ice}\left.\frac{\partial T}{\partial r}\right|_{r=r_F}\right], \qquad [2]$$

$$-\lambda_{ice}\left.\frac{\partial T}{\partial r}\right|_{r=r_S} = C\cdot h_S\cdot T(t, r_S)^{-0.5}\cdot (p_V(t, r_S) - p_V(r_\infty)), \qquad [3]$$

where $\alpha_{ice} = \lambda_{ice}/(\rho_{ice}\cdot c_{ice})$, ρ_{ice}, c_{ice}, and λ_{ice} are the thermal diffusivity, density, specific heat capacity, and thermal conductivity of ice, respectively, $h_{F,w}$ and h_S are the enthalpy of fusion and sublimation of water, respectively, and C is a constant from the Hertz–Knudsen equation (28) (*Stefan Model*). The vapor pressure of the ice–vapor interface is approximated as the saturation pressure for that ice surface temperature, $p_V(t, r_S) \approx p_{V,sat}(T(t, r_S))$, while the vapor pressure at sufficiently large distance from the ice–vapor interface is $p_V(r_\infty) \approx 1$ mbar (*Vapor Pressure Above the Sublimating Surface*). Fig. 3*B* shows a plot of the solution to the above, $(r_S - r_F)$ vs. t, whereby the full solution for a solidifying sphere is used only for the region of the spherical cap that is necessary for this specific case (droplet volume at the moment of freezing 4.2 μL and $\theta_S^* = 96°$) along with experimental values. The ice thickness $(r_S - r_F)$ is scaled by r_S, the total length the phase boundary traverses, and t is scaled with $0.5 r_S^2/(\alpha_{ice} St)$ (Stefan time scale). Here $St = c_{ice}\cdot \Delta T/h_{F,w} = 0.06 \ll 1$ is the Stefan number [$c_{ice} = 2.1$ J/(g K) (29), $h_{F,w} = 334$ J/g (29), and $\Delta T \approx 10$ K, which is the typical average temperature difference observed in simulations and experiments between r_S and r_F (Fig. S2 and Movie S5)]. We see that $(r_S - r_F)$ increases approximately linearly with t, which is a departure from the linear one-dimensional Stefan

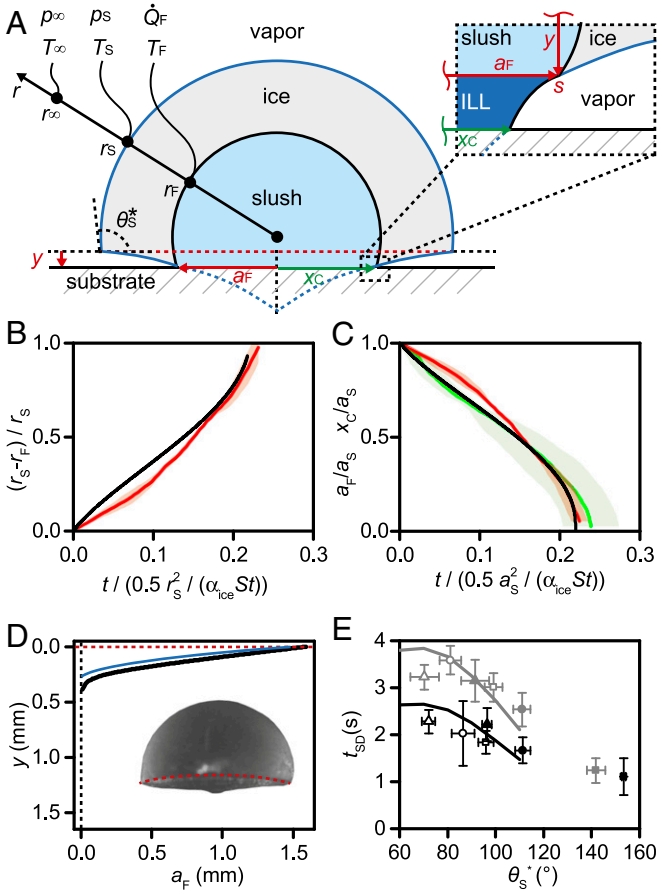

Fig. 3. Effect of liquid–slush–solid–vapor quadri-junction motion on droplet dewetting and dislodging behavior. (*A*) Schematics showing a droplet of radius r_S and contact angle θ_S^* on a substrate (spherical cap), which is freezing due to sublimation. The droplet periphery and core consist of ice (gray) and slush (blue), respectively. The magnified region of the schematic highlights the position of the liquid–slush–solid–vapor quadri-junction, $s(t)=(a_F(t),y(t))$, which is defined as the phase boundary position $r_F(t)$ near the substrate. It also highlights the ILL and its contact radius with the substrate, x_C. (*B*) (r_S-r_F) vs. time t for theoretical (black line) and experimental cases for a freezing droplet on a surface with $\theta_S^*=96°$ and 4.2 μL at the start of freezing (red line; four individual experiments; shaded red region shows the SD). (*C*) a_F vs. t for theoretical (black line) and experimental cases (red line) as well as experimentally measured x_C (green line; five individual experiments; shaded green region shows the SD). (*D*) Plot of s for experimental (blue) and theoretical (black) cases for a droplet on a surface with $\theta_S^*=96°$ and initial volume of 10 μL (*Inset*). (*E*) Simulated (solid lines) and measured self-dislodging times t_{SD} as a function of θ_S^* for two different volumes at the start of freezing: 4.1 ± 0.3 μL (black) and 8.1 ± 0.4 μL (gray). Each point is an average of at least five individual experiments performed on as-purchased PMMA (symbol: open triangle), C_4F_8-treated PMMA (open circle), FDTS-treated PMMA (open square), FDTS-treated hydrophobic glass (solid triangle), nanotextured hydrophobic glass (solid circle), and nanotextured superhydrophobic glass (solid square); error bars indicate the SD.

problem, where the phase boundary progresses as $\propto\sqrt{t}$ (30), and that the experiments and simulation correlate well. With the ability to predict the shape and the position of the phase boundary, we can compute experimental and theoretical values for the radial component of the quadri-junction, s, through the following relation for a spherical cap, $a_F=\sqrt{r_F^2-r_S^2\cos^2(\theta_S^*)}$. It is instructive to compare experimental and theoretical values of a_F with experimental values of x_C, as shown in Fig. 3*C*. We note that they correlate well in time, indicating that the position of the quadri-junction strongly influences the observed dewetting behavior. This link between a_F and x_C is to be expected due to the small thickness of the ILL and the resulting importance of capillary forces: As the quadri-junction moves radially inward (decreasing a_F), a growth in the thickness of the ILL and a reduction in x_C becomes energetically favorable (*ILL*).

As mentioned above, the key to successful self-dislodging is the inward-moving phase boundary, where the free surface solidifies first and the droplet–substrate interface freezes last. This freezing behavior differs from that in ref. 23, where the ice shell formed on the external surface was completely closed (also in the region of contact with the substrate). As a result, the freezing phase boundary in ref. 23 moved inward in a radially symmetric manner, fully enclosing and compressing the (incompressible) liquid core leading to ice-shell fracturing and an explosive shattering of the partially frozen water droplet. In the present work, we found that the frozen shell formed is not completely closed: In the contact region with the substrate the droplet remains liquid. This is responsible for the manifestation of self-dislodging. To this end, we also found that the frozen phase boundary moves inward but asymmetrically, as the base of the drop in contact with the substrate remains unfrozen and provides an exit for the also-unfrozen core of the droplet, alleviating internal stress buildup. The consequence of this though is that the droplet lifts from the substrate. In what follows below, we focus on modeling the lifting motion. During solidification, the droplet should expand due to differences in densities and the incompressibility of the solid and liquid. Here, the expansion breaks symmetry because the free interface freezes before the droplet–substrate interface; therefore, solidification causes mass to be displaced toward the unsolidified droplet–substrate interface. Since the substrate is nonwetting, and the ice–liquid–vapor contact line is pinned, the displaced mass is not expected to spread away from the droplet and wet the surface (*ILL* and Fig. S4). Therefore, the droplet should lift upward. Using the principle of conservation of mass, assuming that the droplet is a spherical cap and that the phase boundary progresses radially inwards (Fig. 3*A*), we estimate the rate of droplet lifting as

$$\frac{dy}{dt}\approx\frac{2r_F\cdot\left(r_F-r_S\cdot\cos\left(\theta_S^*\right)\right)\cdot\dot{r}_F}{a_F^2}\cdot\left(\frac{\nu(1-\phi)-(1-\phi)}{\nu\phi+(1-\phi)}\right), \qquad [4]$$

where ν is the ratio between ρ_{ice} and the density of liquid water. After integration of Eq. **4**, we obtain $y(t)$, which, combined with the previous findings on $a_F(t)$, yields a full solution for the quadri-junction, $s(t)$ (*Quadri-Junction Motion*). Fig. 3*D* shows theoretical and experimental values of s, which compare well, validating the model (Fig. S5). Such profiles are reminiscent of those obtained in freezing droplets on cold substrates, where universal pointy tips are obtained upon full solidification on top, at the center of symmetry of the drop free surface, albeit here the pointed area is inversed and is located at the bottom of the drop (22, 31). To summarize the above findings, Fig. 3*E* plots experimental values of t_{SD} vs. θ_S^* obtained on six different substrates using two different initial droplet volumes. Also included are theoretical predictions of t_{SD}, which is defined as the time it takes for the radial component of the quadri-junction $a_F(t)$ to go from its initial value to zero. The comparison with the simulations shows good agreement for θ_S^* between 70 and 110°, where the model is valid, and a trend of decreasing t_{SD} for rising θ_S^*.

Based on our analysis, we find that droplet contact line motion (dewetting) can be well-predicted with the radial quadri-junction motion; therefore, the time to complete droplet solidification at the droplet–substrate interface can be simply estimated by the Stefan time scale $[0.5a_S^2/(\alpha_{ice}St)]$, and can serve as the design rule when creating icephobic self-dislodging surfaces. For a spherical cap $a_S\propto1/\theta_S^*$ for a given droplet volume, implying that θ_S^* has to be maximized to minimize t_{SD}. Furthermore, for droplet solidification to occur, one should ensure that $\dot{Q}_{sub}\ll\dot{Q}_S,\dot{Q}_F$, which is

achieved by minimizing substrate thermal conductivity, substrate thermal diffusivity, and a_S (*Substrate Heat Transfer* and Figs. S6 and S7). Out of the broad range of substrates self-dislodging occurs on, the above criteria enable us to determine the substrates best suited for robust and fast self-dislodging.

To demonstrate the efficacy of this approach, Fig. 4*A* shows nine water droplets self-dislodging in one experiment from a nanotextured superhydrophobic glass substrate, satisfying the above design criteria. In addition, Fig. 4 *B* and *C* shows water droplet self-dislodging from other technically relevant materials, including stainless steel and poly(methyl methacrylate) (PMMA), designed to be sufficiently hydrophobic and thermally insulating for robust self-dislodging events. To show that self-dislodging can also occur under standard atmosphere environmental pressure conditions and basically requires that heat transfer from the droplet free surface is relatively large to ensure inward solidification, we performed experiments where the droplet was cooled by a cold gas stream at atmospheric pressure—relevant environmental conditions for ice formation. Fig. 4*D* shows a droplet in contact with a nanotextured superhydrophobic glass substrate—in an environment at atmospheric pressure—exposed to a cold nitrogen flow (≈–30 °C, Movie S7). We see that as the droplet freezes, the phase boundary propagates from the outside in, displacing the unsolidified core toward the substrate causing the droplet to lift, reduce substrate contact area, and fully remove from the surface, which is our definition of self-dislodging discussed in detail earlier for vacuum conditions (Fig. 4*D*, *Insets*). This underlines the importance of the self-dislodging mechanism for a wide range of applications where convective heat transfer from the droplet free surface is relevant. Therefore, we demonstrate water droplet self-dislodging on a broad range of material groups, including polymers, ceramics, and metals, both in low- and atmospheric pressure environments and expect that the identification and understanding of the phenomenon herein will pave the way to new approaches in the design of surfaces extremely resistant to ice accretion.

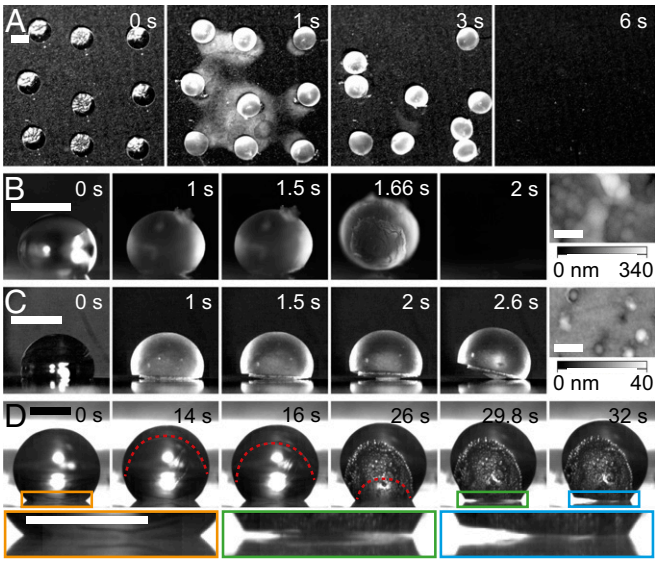

Fig. 4. Robust self-dislodging on several coating compositions. (*A*) Top view: nine water droplets self-dislodging from superhydrophobic glass. The substrate is tilted by 2° with respect to the horizontal position (Movie S6). Fig. 2 (*Inset*) shows the corresponding topographical scan. (*B* and *C*) Droplet self-dislodging from hydrophobic stainless steel and FDTS-treated PMMA, respectively. (*Insets*) Corresponding topographical scans by AFM. (*D*) Self-dislodging from superhydrophobic glass at atmospheric pressure (Movie S7). The droplet is cooled by a stream of cold nitrogen. The dashed red line indicates the position of the freezing front. Magnified contact regions are shown as insets and linked by colored frames. Droplet volume: (*A*–*C*) initially 10 μL; (*D*) initially 5 μL. [Scale bars: (*A*–*C*): 2 mm; (*D*): 1 mm; (*B* and *C*, *Insets*) 500 nm; (*D*, *Insets*) 1 mm).] Scanning electron microscope images of the substrates are presented in Fig. S8.

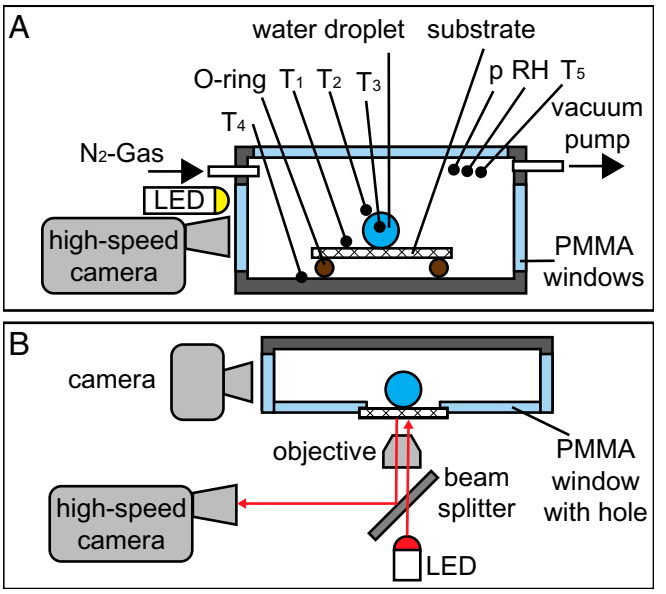

Fig. 5. Schematic of the experimental setup for self-dislodging visualization. (*A*) Configuration for side- and top-view imaging with nitrogen inlet on the left and a connection to vacuum pump on the right. The water droplet is resting on the substrate, which is on a thermally insulating O-ring. Using LED illumination and a high-speed camera, synchronized images and measurements of pressure (*p*), RH, heat flux, and temperature (T1–T5) in the indicated positions are recorded. (*B*) Configuration for high-speed bottom-view visualization through the transparent substrate with additional visualization from the side. The substrate is attached to a PMMA window with a hole. The droplet is placed on the inside of the chamber on the substrate, allowing direct optical access through the substrate. Monochromatic red LED light passes a beam splitter, is focused by an objective, interacts with the droplet substrate interface, and is collected by the high-speed camera.

Materials and Methods

Materials. In this study we used PMMA in thickness of 175 μm and 1 mm obtained from Schlösser GmbH, borosilicate glass (BSG) in thickness 200 μm obtained from Plan Optik AG, as well as sapphire in random orientation in thickness of 200 μm obtained from UQG Ltd. We obtained the 1.4310 stainless steel tape 10 mm wide, 0.1 mm thick, from H+S Präzisions-Folien GmbH. For the chemical functionalization we used 1H, 1H, 2H, 2H-perfluorodecyltrichlorsilane, 96% (FDTS) from Alfa Aesar GmbH, hexane anhydrous 95% from Sigma-Aldrich, isopropyl alcohol (IPA) from Thommen-Furler AG, deionized water (DIW, Merck Milli-Q direct, resistivity >18.2 MΩ cm).

Substrate Preparation. We used the substrates in their as-purchased state, which is hydrophilic, and in their functionalized state, which is hydrophobic. To render the substrates hydrophobic, we treated the substrates with FDTS: First, we used a sputter tool (CS320S; Von Ardenne Dresden) to apply a layer of ∼10-nm silicon dioxide onto the PMMA and the sapphire samples to prepare them for the FDTS treatment. Subsequently, we cleaned and activated all samples in an oxygen plasma (7 min, 100 W; Plasma Asher Diener). We immersed the samples in a mixture of 10 μL FDTS in 20 mL hexane (BSG and sapphire: 2 min; PMMA: 1 min; stainless steel: 2 h), followed by rinsing in hexane (BSG, sapphire, and stainless steel: 1 min; PMMA: 10 s), rinsing in IPA (BSG, sapphire, and stainless steel: 1 min; PMMA: 10 s), rinsing in DIW (BSG, sapphire, and stainless steel: 1 min; PMMA: 10 s), and heating for 10 min on a hotplate (BSG, sapphire, and stainless steel: 120 °C; PMMA: 80 °C). We fabricated the nanotextured, hydrophobic, and superhydrophobic glass samples using maskless reactive ion etching (RIE) for 5 and 120 min, respectively, in an Oxford NPG80 (38 sccm Ar and 12 sccm CHF_3 gas at 200 W). We measured the root-mean-square (rms) roughness of as-purchased BSG by atomic force microscopy (AFM) in three independent scans to be $R_{rms} = 1.1 \pm 0.1$ nm (mean ± SD). After exposure to RIE for 5 and 120 min the roughness increased to $R_{rms} = 3.8 \pm 0.2$ nm and $R_{rms} = 25.7 \pm 0.5$ nm, respectively. The FDTS treatment was the same as for

the not-etched BSG samples. We fabricated the C_4F_8-treated PMMA by exposing the PMMA to a C_4F_8 plasma in a dry etching machine for 10 min (100 sccm, Alcatel AMS 200). Table S1 lists the properties of the substrates including advancing/receding contact angles, θ_a^*, θ_r^*, and the thermal properties.

Experimental Setup. A schematic of the environmental chamber and the data acquisition for side-view visualization is shown in Fig. 5*A*. In the environmental chamber we can reduce the pressure by using a vacuum pump (RZ 2.5; VACUUBRAND), create a dry environment by purging with nitrogen, and reduce for some experiments the temperature on the bottom of the aluminum chamber with the help of a Peltier element. We use a connected pressure sensor (CMR362; Pfeiffer Vacuum), a humidity sensor (IST AG LinPicco A05), and temperature sensors (PT1000 and T-type thermo elements) to record the thermodynamic conditions inside the chamber. We measured heat fluxes with a heat-flux sensor (gSKIN – XM 26 9C calibrated; GreenTEG) applying thermally conductive paste between the bottom of the chamber, the heat flux sensor, and the substrate. We synchronized all signals with the high-speed images with a National Instruments board (NI USB-6361) and the camera software PhotronFastcamViewer. We used a high-speed camera (SA1.1; Photron) at up to 2,000 frames per second and an LED front-side illumination (SL073; Advanced Illumination) to record the self-dislodging event from the side. For bottom-view visualization the experimental chamber was mounted on an inverted microscope setup using the high-speed camera, a 4× objective (Olympus), and a red fiber-coupled LED light source (M625F1; Thorlabs) for the bottom-view visualization through the transparent substrate. A sketch of the inverted microscope setup is shown in Fig. 5*B*. We used an additional camera (DCC1645C; Thorlabs) at 15–30 frames per second for simultaneous side-view visualization.

Experimental Procedure. We used a pipette (20 μL; Eppendorf Research plus) to place water droplets of initial volumes between 5 and 10 μL on the substrate in the chamber. We closed the chamber, purged it with nitrogen to reach a relative humidity below 3%, and opened the valve between the environmental chamber and the vacuum pump.

For the study on the wettability effect, we placed the substrate on an O-ring limiting the heat transfer between the bottom of the chamber and the substrate to a negligible amount. We performed 10 independent experiments per substrate with an initial droplet volume of 10 μL focusing on high-quality side-view visualization and 5 independent experiments per substrate with an initial droplet volume of 5 μL focusing on the visualization of the droplet–substrate interface. For all experiments on the wettability effect, we set the absolute chamber pressure and temperature to be $p_\infty = 2 \pm 1$ mbar and $T_\infty = 23 \pm 2$ °C, respectively, and measure the relative humidity (RH) to be RH = 3%, with an uncertainty of 3% RH, resulting in a low vapor pressure p_V.

For the experiments at atmospheric pressure, we cooled the droplet with a stream of nitrogen vapor directed at the sessile water droplet from above. The nitrogen gas was produced by boiling liquid nitrogen (Kaltgas; KGW Isotherm). The approximate nitrogen vapor temperature impacting onto the droplet was measured with a thermocouple to be -30 ± 5 °C.

Substrate Characterization. To determine the wettability of the substrates, we measured the apparent advancing (θ_a^*) and receding (θ_r^*) water contact angles by inflating (advancing) and deflating (receding) ∼10 μL of water through a flat-tipped plastic needle (GELoader Tips) using a syringe pump (New Era Pump Systems). Using a detector (DCC1645C; Thorlabs), a zoom lens (MVL7000; Thorlabs), and an LED light source, we captured images of the wetting and dewetting dynamics, which we used to measure the contact angles in ImageJ.

We measured the surface roughness with an AFM (Bruker AFM Dimension FastScan) in tapping mode in air.

ACKNOWLEDGMENTS. We thank S. Jung for stimulating discussions, U. Drechsler and P. Eberle for advice on surface fabrication, and J. Vidic, P. Feusi, and N. Delmedico for assistance in experimental setup construction. Partial support by the Swiss National Science Foundation under Grant 162565 and the European Research Council under Advanced Grant 669908 (INTICE) is acknowledged. T.M.S. also acknowledges the ETH Zurich Postdoctoral Fellowship Program and the Marie Curie Actions for People COFUND Programme (FEL-14 13-1).

1. de Gennes PG, Brochard-Wyart F, Quéré D (2004) *Capillarity and Wetting Phenomena: Drops, Bubbles, Pearls, Waves* (Springer, New York), pp 1–32.
2. Bonn D, Eggers J, Indekeu J, Meunier J, Rolley E (2009) Wetting and spreading. *Rev Mod Phys* 81:739–805.
3. Hao C, et al. (2016) Bioinspired interfacial materials with enhanced drop mobility: From fundamentals to multifunctional applications. *Small* 12:1825–1839.
4. Quéré D (2005) Non-sticking drops. *Rep Prog Phys* 68:2495–2532.
5. Nosonovsky M, Bhushan B (2009) Superhydrophobic surfaces and emerging applications: Non-adhesion, energy, green engineering. *Curr Opin Colloid Interface Sci* 14: 270–280.
6. Li X-M, Reinhoudt D, Crego-Calama M (2007) What do we need for a superhydrophobic surface? A review on the recent progress in the preparation of superhydrophobic surfaces. *Chem Soc Rev* 36:1350–1368.
7. Deng X, Mammen L, Butt HJ, Vollmer D (2012) Candle soot as a template for a transparent robust superamphiphobic coating. *Science* 335:67–70.
8. Papadopoulos P, Mammen L, Deng X, Vollmer D, Butt H-J (2013) How superhydrophobicity breaks down. *Proc Natl Acad Sci USA* 110:3254–3258.
9. Kreder MJ, Alvarenga J, Kim P, Aizenberg J (2016) Design of anti-icing surfaces: Smooth, textured or slippery? *Nat Rev Mater* 1:15003.
10. Dalili N, Edrisy A, Carriveau R (2009) A review of surface engineering issues critical to wind turbine performance. *Renew Sustain Energy Rev* 13:428–438.
11. Schutzius TM, et al. (2015) Physics of icing and rational design of surfaces with extraordinary icephobicity. *Langmuir* 31:4807–4821.
12. Boinovich LB, Emelyanenko AM (2013) Anti-icing potential of superhydrophobic coatings. *Mendeleev Commun* 23:3–10.
13. Alizadeh A, Bahadur V, Kulkarni A, Yamada M, Ruud JA (2013) Hydrophobic surfaces for control and enhancement of water phase transitions. *MRS Bull* 38:407–411.
14. Jung S, et al. (2011) Are superhydrophobic surfaces best for icephobicity? *Langmuir* 27:3059–3066.
15. Eberle P, Tiwari MK, Maitra T, Poulikakos D (2014) Rational nanostructuring of surfaces for extraordinary icephobicity. *Nanoscale* 6:4874–4881.
16. Boreyko JB, Chen C-H (2009) Self-propelled dropwise condensate on superhydrophobic surfaces. *Phys Rev Lett* 103:184501.
17. Bird JC, Dhiman R, Kwon H-M, Varanasi KK (2013) Reducing the contact time of a bouncing drop. *Nature* 503:385–388.
18. Liu Y, et al. (2014) Pancake bouncing on superhydrophobic surfaces. *Nat Phys* 10: 515–519.
19. Maitra T, et al. (2014) On the nanoengineering of superhydrophobic and impalement resistant surface textures below the freezing temperature. *Nano Lett* 14:172–182.
20. Jung S, Tiwari MK, Poulikakos D (2012) Frost halos from supercooled water droplets. *Proc Natl Acad Sci USA* 109:16073–16078.
21. Jung S, Tiwari MK, Doan NV, Poulikakos D (2012) Mechanism of supercooled droplet freezing on surfaces. *Nat Commun* 3:615.
22. Marín AG, Enríquez OR, Brunet P, Colinet P, Snoeijer JH (2014) Universality of tip singularity formation in freezing water drops. *Phys Rev Lett* 113:054301.
23. Wildeman S, Sterl S, Sun C, Lohse D (2017) Fast dynamics of water droplets freezing from the outside in. *Phys Rev Lett* 118:084101.
24. Kim P, et al. (2012) Liquid-infused nanostructured surfaces with extreme anti-ice and anti-frost performance. *ACS Nano* 6:6569–6577.
25. Schutzius TM, et al. (2015) Spontaneous droplet trampolining on rigid superhydrophobic surfaces. *Nature* 527:82–85.
26. Pruppacher HR, Klett JD (2010) *Microphysics of Clouds and Precipitation* (Springer, Dordrecht, The Netherlands), pp 659–699.
27. Tabakova S, Feuillebois F, Radev S (2010) Freezing of a supercooled spherical droplet with mixed boundary conditions. *Proc R Soc A Math Phys Eng Sci* 466:1117–1134.
28. Kossacki KJ, Leliwa-Kopystynski J (2014) Temperature dependence of the sublimation rate of water ice: Influence of impurities. *Icarus* 233:101–105.
29. Lide DR, ed (2005) *CRC Handbook of Chemistry and Physics* (CRC Press, Boca Raton, FL), 85th Ed.
30. Rubinshteĭn LI (1971) *The Stefan Problem* (American Mathematical Society, Providence, RI), Vol 27, pp 18–38.
31. Ajaev VS, Davis SH (2004) The effect of tri-junction conditions in droplet solidification. *J Cryst Growth* 264:452–462.
32. Udd E (2011) *Light Sources. Fiber Optic Sensors* (John Wiley & Sons, Hoboken, NJ), pp 35–62.
33. Brakke KA (1992) The surface evolver. *Exp Math* 1:141–165.
34. Buck AL (1981) New equations for computing vapor pressure and enhancement factor. *J Appl Meteorol* 20:1527–1532.